Article

Preparation of Heterojunctions Based on $Cs_3Bi_2Br_9$ Nanocrystals and G-C_3N_4 Nanosheets for Photocatalytic Hydrogen Evolution

María Medina-Llamas[1,2*] Andrea Speltini[2], Antonella Profumo[2], Francesca Panzarea[3], Antonella Milella[3], Francesco Fracassi[3,4], Andrea Listorti[3] and Lorenzo Malavasi[2*]

[1] Unidad Académica Preparatoria, Plantel II, Universidad Autónoma de Zacatecas, Zacatecas, 98068, México; maría.medina@uaz.edu.mx
[2] Department of Chemistry, University of Pavia, Via Taramelli 12, 27100 Pavia, Italy; andrea.speltini@unipv.it, antonella.profumo@unipv.it, lorenzo.malavasi@unipv.it
[3] Department of Chemistry, University of Bari "Aldo Moro" via Orabona 4, Bari 70126, Italy; andrea.listorti@uniba.it, f.panzarea2@studenti.uniba.it
[4] National Research Council, Institute of Nanotechnology (CNR-NANOTEC), Department of Chemistry, 70125 Bari, Italy, francesco.fracassi@uniba.it
* Correspondence: MML maría.medina@uaz.edu.mx; LM lorenzo.malavasi@unipv.it

Abstract: Heterojunctions based on metal halide perovskites (MHPs) are promising systems for photocatalytic hydrogen evolution reaction (HER). In this work, we coupled $Cs_3Bi_2Br_9$ nanocrystals (NCs), obtained by wet ball milling synthesis, with g-C_3N_4 nanosheets (NSs) produced by thermal oxidation of bulk g-C_3N_4 in air. These methods are reproducible, inexpensive, and easy to scale up. Heterojunctions with different loadings of $Cs_3Bi_2Br_9$ NCs were fully characterized and tested for HER. A relevant improvement of H_2 production with respect to pristine carbon nitride was achieved at low NCs levels reaching values up to about 4600 μmol g^{-1} h^{-1}. This work aims to provide insights on the synthesis of inexpensive and high performing heterojunctions using MHP for photocatalytic applications.

Keywords: lead-free perovskites; hydrogen evolution; photocatalysis, carbon nitride, perovskites, ball milling

1. Introduction

In recent times, the field of application of metal halide perovskites (MHPs) has been extended to photocatalysis thanks to their excellent optical properties such as high optical absorption coefficient, high carrier mobility and long electron–hole diffusion lengths [1]. In this vast area of applications, ranging from hydrogen photogeneration to carbon dioxide reduction and organic dye degradation[2-4], the need of using lead-free materials is a key aspect by considering the final aims of such uses of MHPs. In general, lead is replaced by elements with similar electronic structure and/or comparable ionic radius, such as Sn^{2+}, Ge^{2+}, Sb^{3+} or Bi^{3+}. To date, several examples of the use of lead-free MHPs in photocatalysis have been reported[5-7]. Among these results, a class of interesting phases, showing good performances, is the one of $Cs_3Bi_2X_9$ perovskites derivatives. By way of example, Bresolin et *al.* (2020) produced bulk $Cs_3Bi_2I_9$ by a precipitation method and tested it for the photocatalytic degradation of dyes [8]. The same application was explored by Akinbami et *al.* (2021) by using $Cs_3Bi_2Br_9$ nanocrystals (NCs) prepared by a hot injection method, while [9] Bhosale et *al.* (2019) synthetized $Cs_3Bi_2Br_9$ NCs via ultrasonication for the photoreduction of carbon monoxide [10]. In general, a further enhancement of the MHPs photocatalytic activity is achieved by using them in combination with a second semiconductor as commonly done in current research, i.e., by creating heterojunctions. Among other visible-

 doi:10.20944/preprints202211.0524.v1

light active catalysts, graphitic carbon nitride (g-C_3N_4) has been already advantageously used to create composite systems with lead-free MHPs [11, 12].

g-C_3N_4, is a 2D layered material that has rapidly emerged as a promising photocatalyst. It can be easily synthesized from the thermal polycondensation of inexpensive precursors that contain nitrogen and carbon atoms such as: dicyanamide, cyanamide, melamine, urea and thiourea. Its suitable bandgap, ~2.8 eV, makes it active in the visible solar spectrum. It is a thermally and chemically stable compound, resistant to acid or alkaline conditions. On the other hand, g-C_3N_4 has a high recombination rate of its electron-hole pairs and low surface area. The first drawback, is due to the presence of defects as a result of an incomplete deamination during the thermal condensation process [13]. These defects act as recombination centres, leading to the decrease of the photocatalytic activity of the material. The low surface area of g-C_3N_4 can be overcome by exfoliation methods such as: thermal, ultrasonic or chemical exfoliation [14-16]. Thanks to these strategies, it is possible to obtain g-C_3N_4 nanosheets (g-C_3N_4 NSs) that have high aspect-ratio, thin thickness and plenty of surface groups for the anchoring of co-catalysts [17]. Consequently, exfoliation methods are widely used to increase the surface area of bulk g-C_3N_4. Among them, ultrasonication is an energy and time consuming process that usually does not produce single layers of g-C_3N_4 [17]. Chemical exfoliation is achieved using strong acids (H_2SO_4 and/or HNO_3) but is time-consuming. By contrast, thermal exfoliation is a low-cost, easy scale-up and environmentally friendly method to obtain single layers [18].

Our research group recently explored the use of bulk g-C_3N_4 in the construction of heterojunctions with microcrystalline $Cs_3Bi_2Br_9$ for hydrogen production, achieving a hydrogen evolution rate (HER) production up to about 1050 μmol g^{-1} h^{-1} compared to 81 μmol g^{-1} h^{-1} of bulk g-C_3N_4 [17]. Based on these results, we decided to further investigate this heterojunction to boost the production of hydrogen through the combination of nanocrystalline $Cs_3Bi_2Br_9$ and g-C_3N_4 NSs. The aim is to obtain nanostructured composites that can be easily manufactured at large scale using simple preparation routes. For this purpose, the $Cs_3Bi_2Br_9$ NCs where synthesised by wet ball milling instead of using standard liquid-phase strategies that require high-temperature (130 °C - 220 °C), inert gas atmosphere and the use of large quantities of organic solvents (i.e., hot injection or ligand-assisted reprecipitation)[20]. Indeed, these methods produce small quantities of NCs that need further purification, making the whole process expensive, energy consuming and not in line with green chemistry principles. To overcome the former disadvantages, a mechano-chemical procedure using a planetary ball miller was chosen in this work. By this method, the synthesis of perovskites takes place primarily via high-energy impacts between the grinding balls and the grinding bowl (which contains the perovskite precursors). The grinding balls move across the bowl at high speed and hit the perovskite precursors, resulting into the mechanical downsizing and the chemical reaction of the perovskite precursors [21]. Ball milling synthesis can be conducted without solvents (dry synthesis) and with solvents (wet synthesis). Both approaches are reproducible and scalable. Wet ball milling (WBM) is a green chemistry synthesis method and does not require inert atmosphere or high temperature [22]. The experiments conducted in this research were carry out using a laboratory-scale ball mill in a batch mode, unlike industrial ball mills which operate in a continuous mode [23], thus a high synthesis throughput can be easily achieved.

Based on the previous considerations, the strategy used in the present work to overcome the limitations of bulk g-C_3N_4 is based on increasing its surface area by a thermal exfoliation process followed by the construction of a heterojunction with $Cs_3Bi_2Br_9$ NCs via wet ball milling. As already demonstrated for a similar bulk heterojunction [5], there is a favourable band-alignment between the two semiconductors that promotes charge transfer and reduces the charge recombination rate of g-C_3N_4. In addition to this, the nanostructured morphology of the present heterojunction is expected to provide a more efficient route for the photocatalytic activity of the $Cs_3Bi_2Br_9$ NCs/g-C_3N_4 NSs composites.

 doi:10.20944/preprints202211.0524.v1

2. Materials and Methods

2.1 Synthesis of bulk g-C_3N_4 and g-C_3N_4 Nanosheets

Bulk g-C_3N_4 was synthetized by the polymerization of dicyandiamide (DCD, Aldrich, 99%) using a thermal treatment under N_2 flux. In the process an alumina crucible was completely filled with DCD and heated up to 550° C with a ramp of 1°C/min and a dwell time of 4 h, followed by a cooling step to room temperature. Later, the bulk g-C_3N_4 was finely ground with a mortar and a pestle. The g-C_3N_4 NSs were obtained by subjecting the bulk g-C_3N_4 to a second calcination in air. The calcination of 500 mg of bulk g-C_3N_4 at 500° C with a ramp of 5°C/min and 2 h of dwell was performed, as reported in a previous publication [15].

2.2 Synthesis of bulk $Cs_3Bi_2Br_9$ and $Cs_3Bi_2Br_9$ NCs

The $Cs_3Bi_2Br_9$ bulk perovskite was prepared by a solid-state synthesis using a planetary milling (Fritsch, pulverisette 7). 1.5 g of $Cs_3Bi_2Br_9$ bulk perovskite was prepared by adding the stochiometric quantities of caesium bromide (CsBr, Sigma Aldrich 99.9 %) and bismuth bromide III ($BiBr_3$, Sigma Aldrich 99 %) in each tungsten carbide grinding bowl was prepared. Then, fifteen tungsten carbide balls (D= 5 mm) were added into each grinding bowl to achieve a ratio of 10 balls/g_{solids}. The milling was performed in 3 cycles of 20 minutes at 500 rpm with a 10 min pause between each cycle. $Cs_3Bi_2Br_9$ nanocrystals (NCs) were produced by a LARP (ligand assisted reprecipitation) method using a planetary milling. For the synthesis 0.07 mmol of the previously synthesized $Cs_3Bi_2Br_9$ bulk perovskite, 0.1 ml oleic acid (OA, Sigma Aldrich 99 %), 0.1 ml oleylamine (OLA, Sigma Aldrich 98 %) and 0.8 ml toluene (Sigma Aldrich, 99.5 %) were addedin a tungsten carbide bowl. For this step a ratio of 40 balls/g_{solids} was selected. The milling was carried out with 2 cycles of 15 minutes at 500 rpm with a 10 min pause between the cycles. The synthesis of the $Cs_3Bi_2Br_9$ NCs was easily scaled up by adding more reagents while keeping the ratio of 40 balls/g_{solids}. The obtained suspension was retrieved from the grinding bowls and subjected to centrifugation at 8 500 rpm for 10 min to remove the excess of ligands. The supernatant was discarded and the NCs were redispersed in fresh toluene. This step was repeated two more times. Next, the NCs suspension was subjected to a mild centrifugation at 3 000 rpm to remove large aggregates. Finally, the supernatant containing the $Cs_3Bi_2Br_9$ NCs was carefully retrieved.

2.3 Synthesis of $Cs_3Bi_2Br_9$ NCs/ g-C_3N_4 Nanosheets

The composites between $Cs_3Bi_2Br_9$ NCs and g-C_3N_4 NSs were produced via a wet chemistry step by mixing the $Cs_3Bi_2Br_9$ NCs suspended in toluene with g-C_3N_4 NSs, previously sonicated for 10 min in fresh toluene. The system was kept under agitation at 500 rpm and heated up to 50° C until a complete evaporation of the solvent was achieved. Nominal amounts of NCs loading on g-C_3N_4 NSs were 0.05, 0.5, 1 and 1.5 %. %. The effective loading was determined by acidic dissolution followed by inductively coupled plasma-optical emission spectroscopy (ICP-OES) quantitation of the bismuth content, as described below.

2.4 Characterization

The crystal structure of the samples was acquired at room temperature Cu-radiation XRD using a Bruker D2 diffractometer. Diffuse reflectance spectroscopy spectra were obtained in the wavelength range 250-850 nm using a Jasco V-750 spectrophotometer, equipped with an integrating sphere (Jasco ISV-922). Microstructural characterization of the samples was achieved via a high-resolution scanning electron microscope (SEM, TESCAN Mira 3) operated at 20 kV. Surface area measures were carried out via Brunauer,

 doi:10.20944/preprints202211.0524.v1

Emmett and Teller (BET) single point method using a Flowsorb II 2300 (Micromeritics, US) apparatus. Each sample was accurately weighed (0.3 g) and degassed at 80 °C for 15 hours under a continuous stream of N_2:He 30:70 mixture. Gas adsorption was achieved by placing the sample in liquid nitrogen. TEM micrographs of $Cs_3Bi_2Br_9$ NCs were obtained by means of a JEOL JEM-1200 EX II microscope operating at 100 kV, equipped with a tungsten filament as electron source.

Quantification of the amount of perovskite in the composites was achieved by determination of bismuth by ICP-OES (Perkin Elmer Optima 3300 DV) after complete dissolution of the perovskite fraction. In detail, 10 mg of each composite and 2 mL of concentrated HNO_3 (69 %, Fisher, ICP-OES, for Trace Metal Analysis) were placed in glass vessels (beakers). The suspension was kept under agitation for 3 h, under reflux conditions. Later, the beakers were left open, the temperature was slightly increased to evaporate most of the acid. Subsequently, 8 mL of tri-distilled water were carefully added to each glass vessel to decrease the acidity of the suspension. Finally, the suspension was filtrated on a 0.45 μm nylon membrane (syringe filter unit, Whatman) and made up to final volume of 10 ml distilled water. The entire process was carried out under the fume hood. The weight percentage of the perovskite in the composites was determined by the quantification of bismuth in the obtained solutions by external calibration; Bi standard solutions were prepared in distilled water 1% v/v ultrapure HNO_3, in the concentration range 1-50 mg L^{-1}.The photoluminescence (PL) measurements were recorded by means of a Fluorolog®-3 spectrofluorometer (HORIBA Jobin-Yvon), equipped with a 450 W xenon lamp as exciting source and double grating excitation and emission monochromators. All the optical measurements were performed at room temperature on powder dispersed samples as-obtained from the synthesis without any size sorting treatment. The PL emission spectra were recorded by using an excitation wavelength of 350 nm. Time-Resolved PL (TRPL) measurements were carried out by Time Correlated Single Photon Counting (TCSPC) technique, with a FluoroHub (HORIBA Jobin-Yvon). CDs solutions were excited using 80 ps laser diode sources at 375 nm (NanoLED 375L). Time resolution was ~300 ps for all the measurements.

Surface chemical composition was investigated by XPS analyses with a PHI 5000 Versa Probe II spectrometer (Physical Electronics) equipped with a monochromatic Al Kα X-ray source (1486.6 eV), operated at 15 kV and 24.8 W, with a spot size of 100 μm. Survey (0–1400 eV) and high-resolution spectra (C1s, O1s, N1s, Br3d Cs3d and Bi4f) were recorded in FAT (Fixed Analyser Transmission) mode at a pass energy of 117.40 and 29.35 eV, respectively. Surface charging was compensated using a dual beam charge neutralization system. The hydrocarbon component of C1s spectrum was used as internal standard for charging correction and it was fixed at 284.8 eV. Spectra were processed with MultiPak software (Physical Electronics).

2.5 Photocatalytic hydrogen experiments

Hydrogen evolution experiments took place in Pyrex glass containers (32 mL) containing 24 mL of a10 % (*v*/*v*) triethanolamine aqueous solution (pure TEOA from Aldrich, ≥ 99%) and 24 mg of the photocatalyst (1 g $_{catalyst}$/L $_{solution}$). Oxygen was removed by argon bubbling for 20 min. Prior to sealing the glass containers with sleeve stopper septum, platinum was added as a co-catalyst, by pouring 40 μL of a 0.08 M H_2PtCl_6 solution (chloroplatinic acid hydrate, 38 % Pt basis, Sigma Aldrich), using a 10-100 μL micropipette. When starting irradiation, platinum is photo-reduced and *in situ* photodeposited on the catalyst surface. Irradiation was performed under simulated solar light (1500 W Xenon lamp, 300-800 nm, IR-treated soda lime glass UV outdoor filter) at 500 W m^{-2} for 6 hours under magnetic stirring, using a Solar Box 1500e (CO.FO.ME.GRA S.r.l.). Triplicate experiments were performed on all samples. The headspace evolved gas was quantified by gas chromatography coupled with thermal conductivity detection (GC-TCD). The HER is expressed as μmol per gram of catalyst per hour of irradiation (μmol g^{-1} h^{-1}) [7].

 doi:10.20944/preprints202211.0524.v1

3. Results and Discussion

A set of composites consisting of $Cs_3Bi_2Br_9$ NCs and g-C_3N_4 NSs with different perovskite loadings were prepared according to the procedure described in the Experimental section. The effective weight percentage of perovskite in each composite was calculated through the Bi content measured by ICP-OES (as described in Section 2.4). The percentages of perovskite loading, in terms of % weight, in the final composites 0.02, 0.44, 0.91 and 1.47 % were in good agreement with nominal starting values of 0.05, 0.5, 1 and 1.5 %. The composites were extensively characterized in terms of crystal structure, optical properties, and morphology.

Figure 1 shows the X-ray diffraction patterns of all prepared materials, with the g-C_3N_4 NSs at the bottom of the figure, followed by the XRD pattern of the composites and the pattern of $Cs_3Bi_2Br_9$ NCs at the top of the figure. g-C_3N_4 pattern is characterized by the broad peak at approximately 27° which is clearly visible in all the patterns of the composites being carbon nitride the main phase. The contribution of the $Cs_3Bi_2Br_9$ NCs to the patterns can only be slightly appreciated at the two highest loadings (0.91 and 1.47 wt. %) where some intensities at about 22.0° and 31.6° can be found corresponding to the (102) and (202) planes, respectively. Fig. S1 compares the X-ray diffraction pattern of bulk g-C3N4 and g-C3N4 NSs Both samples, have the main peaks at 13° and 27° that correspond to the in-plane structural packing motifs (100) and the interlayer stacking of the conjugated aromatic systems (002), respectively [14]. Both peaks become broader and less pronounced for the g-C_3N_4 NSs, suggesting a decrease of size in both directions (i.e., parallel, and vertical to the C_3N_4 layers) caused by the thermal oxidation process and a partial loss of structural order in the planes.

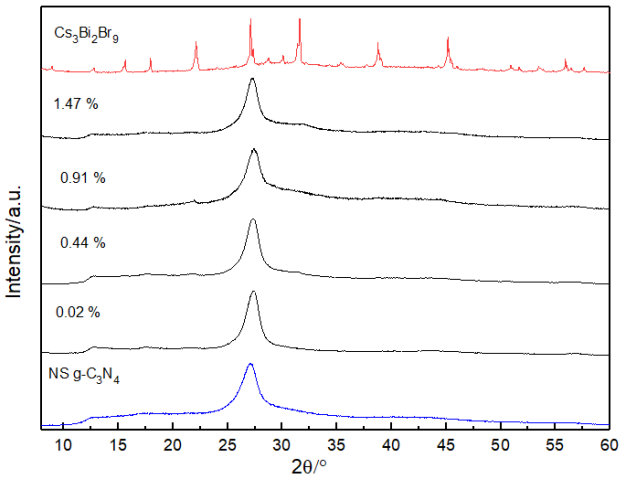

Figure 1. X-ray diffraction patterns of the g-C_3N_4 nanosheets, the $Cs_3Bi_2Br_9$ NCs and the $Cs_3Bi_2Br_9$ NCs/g-C_3N_4 NSs composites produced at different percentages of perovskite loading (% *wt*).

The morphology and microstructure of the g-C_3N_4 NSs were investigated by SEM and TEM as shown in Figure 2a and Figure 2b. Figure 2a confirms that the g-C_3N_4 NSs consist of agglomerates of thin sheets that tend to bend at the edges. The TEM micrograph (Fig. 2b) demonstrates the formation of nanosheets due to the thermal exfoliation process that weakens the bonds between the layers of bulk g-C_3N_4. The yield of the thermal exfoliation process was 59 %, it was measured as the ratio between the obtained mass of g-C_3N_4 NSs and the initial mass of bulk g-C_3N_4. The resulting specific surface area (SSA) values of the g-C_3N_4 NSs was 103.5 m^2/g, whereas the SSA of the bulk g-C_3N_4 was 11.7 m^2/g. This is almost a nine-fold increase in the SSA achieved by thermal exfoliation. For comparison, Fig. S2 shows a low magnification SEM micrograph of the bulk g-C_3N_4, showing, for the bulk material, a more compact microstructure. Figure 2c and Figure 2d show,

 doi:10.20944/preprints202211.0524.v1

as selected examples, the backscattered electron (BSE) micrographs of the 0.44 % and 1.47 % *wt.* $Cs_3Bi_2Br_9$ NCs/g-C_3N_4 NSs. In addition, in the inset of Fig. 2c, it is shown a TEM image of the starting $Cs_3Bi_2Br_9$ NCs having an average size around 4-5 nm. The small particle size is achieved thanks to the mechanical downsizing by WBM and the presence of ligands that prevent the growth of the NCs. Both BSE-HRSEM micrographs show a homogeneous distribution of small $Cs_3Bi_2Br_9$ NCs over the 2D nanosheets and the presence of few clusters of $Cs_3Bi_2Br_9$ NCs of different sizes. Agglomerations of NCs might occurred during the preparation of the composite. However, small particles of $Cs_3Bi_2Br_9$ can be easily seen, especially in Figure 2d. Higher magnification SEM image of 0.44 % *wt.* sample is reported in the supporting information (Fig. S4) showing in greater detail the homogenous distribution of $Cs_3Bi_2Br_9$ NCs.

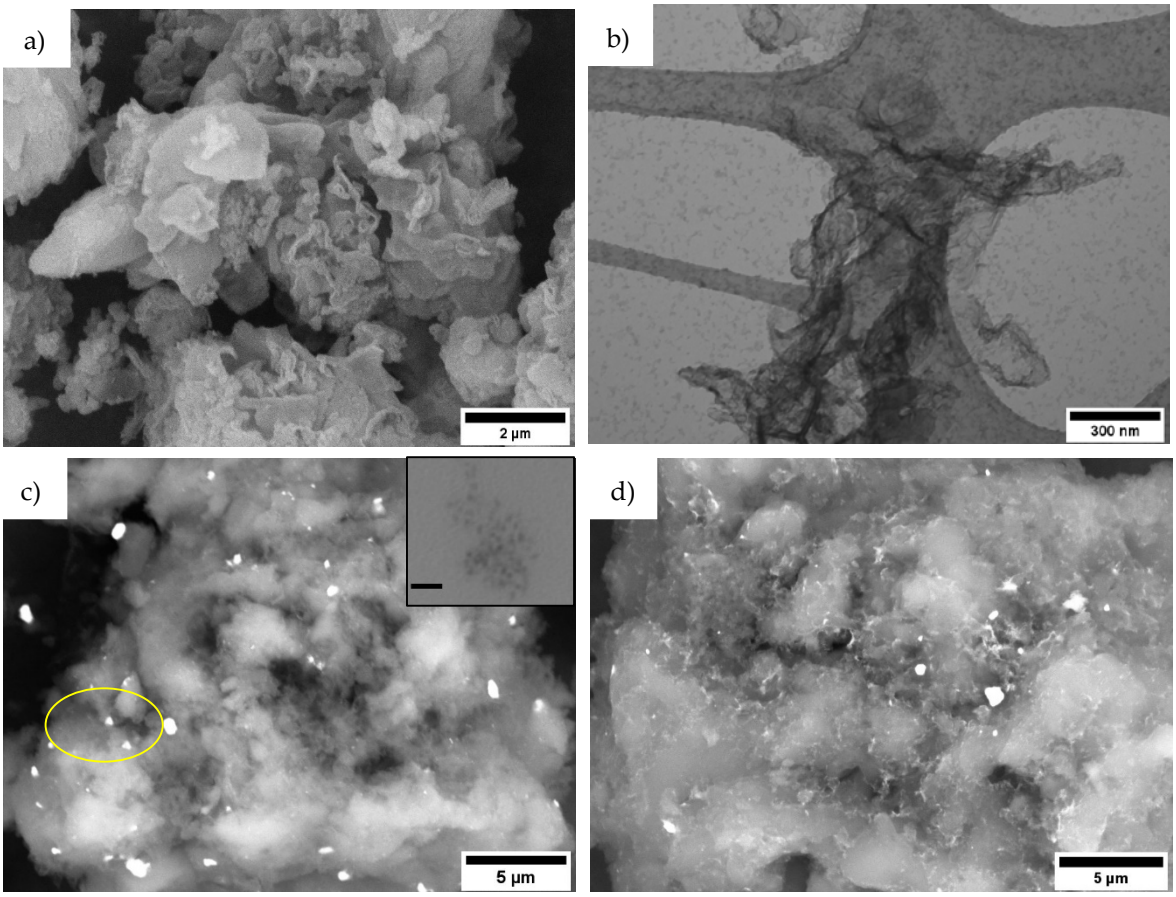

Figure 2. a) SEM and b) TEM micrograph of the g-C_3N_4 NSs, c) BSE-HRSEM of the 0.44 % wt. $Cs_3Bi_2Br_9$ NCs/g-C_3N_4 NSs, d) close up of the yellow area. Inset: TEM micrograph of the $Cs_3Bi_2Br_9$ NCs (scale bar 20 nm).

Optical properties of the $Cs_3Bi_2Br_9$ NCs/g-C_3N_4 NSs composites were determined by UV–Vis absorption spectroscopy. Figure 3a show the Tauc plots for each material, the estimated band gap for the nanosheets of g-C_3N_4 was 2.82 eV. The addition of $Cs_3Bi_2Br_9$ NCs to the nanosheets g-C_3N_4 produced a slight shift towards lower energies with the band gaps moving around 2.78 eV. Fig. S3 shows the absorbance spectra versus wavelength of all samples. Figure 3b shows the normalized photoluminescence spectra of $Cs_3Bi_2Br_9$ NCs/g-C_3N_4 NSs composites measured in the range 360-680 nm, compared with bare g-C_3N_4 and $Cs_3Bi_2Br_9$ NCs spectra. Pure g-C_3N_4 shows an emission peaked at 459 nm. Compared to it, no shift of the emission peak or change in the peak shape is observed for all the samples, suggesting that a perovskite loading of this entity does not affect the steady state emission properties characterized by a dominating g-C_3N_4 contribution. The time resolved photoluminescence decay curves of the same samples are shown in Fig 3b. It is

Preprints (www.preprints.org) | NOT PEER-REVIEWED | Posted: 29 November 2022 doi:10.20944/preprints202211.0524.v1

possible to notice that charge lifetime slightly decreases upon introduction of $Cs_3Bi_2Br_9$ NCs. By the multi-exponential fitting it can be estimated that the lifetime of bare g-C_3N_4 is 12.5 ns, while those of $Cs_3Bi_2Br_9$ NCs/g-C_3N_4 NSs composites are respectively 9.6, 9.1, 8.9 and 8.7 ns with increasing amount of perovskite loading. These decreasing lifetimes suggest how differences occurs in the relative populations of excitation/deactivation processes when increasing amount of perovskite NCs are loaded on g-C_3N_4 NSs. As we previously found for parental systems this peculiar optical behaviour of perovskite/carbon nitride composites could be associated to excitation/deactivation paths funnelling generated charges upon localized states [19].

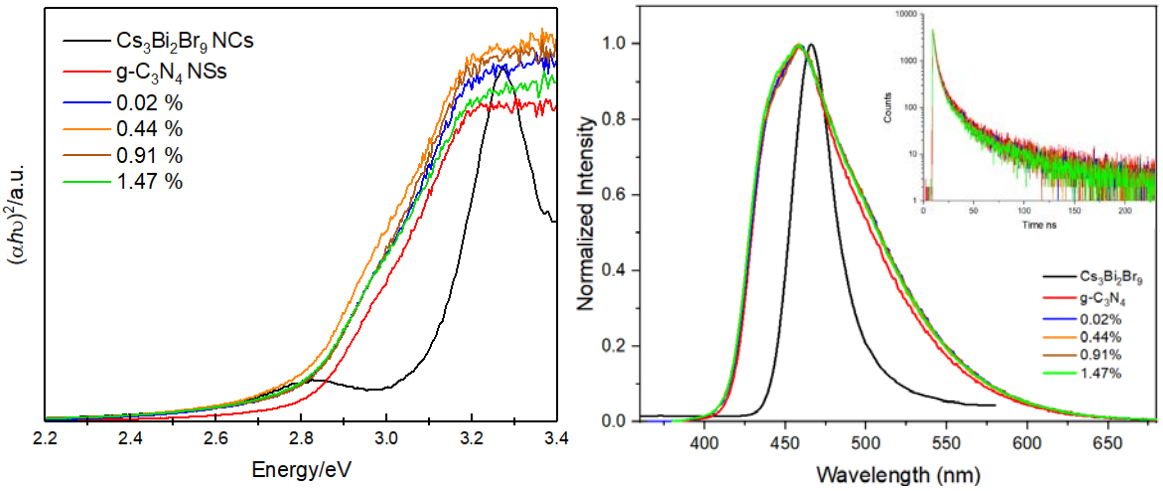

Figure 3. a) Tauc plot of the g-C_3N_4 NSs, the $Cs_3Bi_2Br_9$ NCs and the $Cs_3Bi_2Br_9$ NCs/g-C_3N_4 NSs composites produced at different percentages of perovskite loadings (% *wt*), b) normalized emission and time-resolved photoluminescence spectra of the g-C_3N_4 NSs, the $Cs_3Bi_2Br_9$ NCs and the $Cs_3Bi_2Br_9$ NCs/g-C_3N_4 NSs composites (λ_{ex} = 350 nm).

Surface chemical composition of composites was investigated by XPS analyses. Figure 4 reports the Bi4f high resolution spectrum of a representative sample (0.02 % *wt.* $Cs_3Bi_2Br_9$/g-C_3N_4 NSs). The $Bi4f_{7/2}$ component is peaked at 159.0 eV confirming the presence of the perovskite component in the composite and the Bi^{3+} oxidation state.

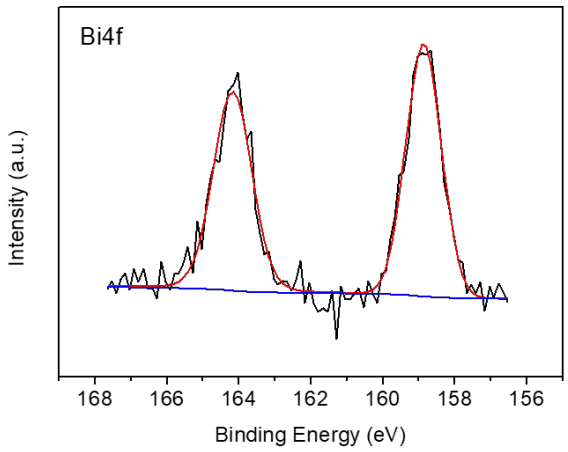

Figure 4. Bi4f high resolution spectrum from XPS analyses of the composite sample 0.02 % *wt.* $Cs_3Bi_2Br_9$ NCs/g-C_3N_4 NSs.

The solar-driven photocatalytic efficiency of the prepared composites was determined in terms of hydrogen evolution reaction (HER) under standard test conditions, *viz.*

 doi:10.20944/preprints202211.0524.v1

10 % *v/v* TEOA aqueous solution, as a sacrificial agent, and 3 % *wt*. platinum as co-catalyst. Fig. 5 shows the HER results as a function of perovskite loading. HER of the g-C_3N_4 NSs achieved a very high value of 3212 μmol g^{-1} h^{-1}, is most probably related to the high surface area achieved by thermal exfoliation of bulk g-C_3N_4. The incorporation of $Cs_3Bi_2Br_9$ NCs into the g-C_3N_4 NSs resulted in a positive increase in the hydrogen photogeneration with mean values of 4593, 4173 and 3595 (n=3) when the loading of the perovskite in the composite was 0.02, 0.44 and 0.91 % *wt*., respectively. These results clearly indicate a synergic effect between the two semiconductors ($Cs_3Bi_2Br_9$ NCs and g-C_3N_4 NSs). However, higher perovskite loadings resulted in a detrimental effect to HER, with the composite prepared at the highest perovskite loading (1.47 % *wt*.) producing just 1674 μmol g^{-1} h^{-1}.

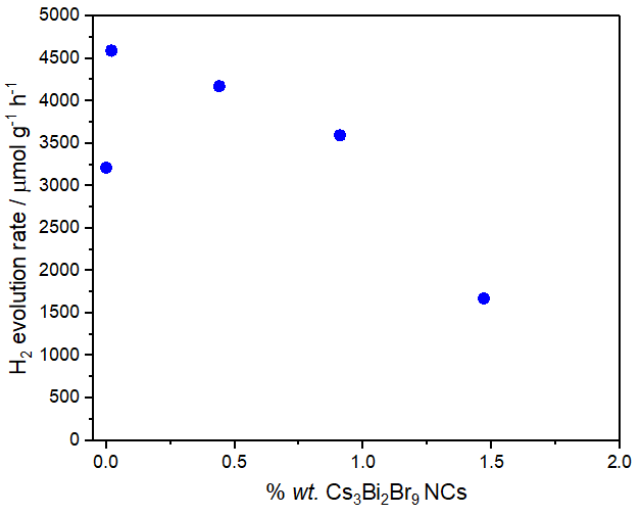

Figure 5. Hydrogen evolution reaction of the $Cs_3Bi_2Br_9$ NCs/g-C_3N_4 NSs composites observed at different percentages of perovskite loading (% *wt*.); conditions: 10 % *v/v* TEOA aqueous solution, 1 g L^{-1} catalyst,3 % *wt*. Pt co-catalyst, simulated solar light (6 h, 500 W m^{-2}); RSD < 10 % (n = 3).

As mentioned in the introduction, we previously investigated the analogous heterojunction made of microcrystalline $Cs_3Bi_2Br_9$ and bulk g-C_3N_4 (not exfoliated), reporting a HER of 81 μmol g^{-1} h^{-1} for bulk carbon nitride, 22 μmol g^{-1} h^{-1} for the pure microcrystalline perovskite and the highest H_2 production around 1050 μmol g^{-1} h^{-1} achieved for the 2.5 % *wt*. bulk $Cs_3Bi_2Br_9$ /bulk g-C_3N_4 composite, accompanied by a decrease of the HER when the loading of the perovskite exceeded 2.5 % wt. [19]. A similar trend in the synergistic effect between the two semiconductors is also observed here but with a shift of the maximum hydrogen photogeneration achieved at lower perovskite amounts, indicating a more efficient charge transfer at the interface between $Cs_3Bi_2Br_9$ and g-C_3N_4 when nanostructured semiconductors are employed in the construction of the heterojunction. Based on available electronic structure data, the proposed mechanism of the actual band alignment between $Cs_3Bi_2Br_9$ and g-C_3N_4 in the present heterojunction (Type II) is shown in Figure 6 [24-26].

Preprints (www.preprints.org) | NOT PEER-REVIEWED | Posted: 29 November 2022 doi:10.20944/preprints202211.0524.v1

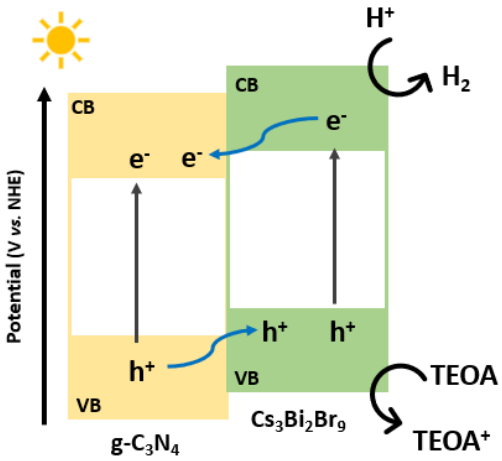

Figure 6. Diagram of charge transfer in the $Cs_3Bi_2Br_9$ NCs/g-C_3N_4 NSs heterojunction for the photocatalytic H_2 production under solar radiation.

Such an alignment favours efficient charge separation leading to the migration of the photogenerated holes from g-C_3N_4 to $Cs_3Bi_2Br_9$ and, in turn, of the photogenerated electrons from $Cs_3Bi_2Br_9$ to g-C_3N_4 resulting in an improvement of the HER in the heterojunction. The trend of the HER with the perovskite loading can be explained based on the self-trapping phenomena occurring in $Cs_3Bi_2Br_9$ at higher concentrations because of polaron formation which seems to be an inactive mechanism at lower amounts of perovskite [13].

Finally, Table 1 lists the series of lead-free MHPs-based heterojunctions with g-C_3N_4 reported to date in the current literature for the photogeneration of hydrogen.

As can be seen, a relevant improvement in the H_2 production can be easily reached when moving from a bulk to a nanostructured system, with a concomitant decrease the perovskite loading in the best-performing composition.

5. Conclusions

In the present work we synthesized $Cs_3Bi_2Br_9$ nanocrystals by a LARP method coupled with a planetary milling process. These NCs were coupled to g-C_3N_4 nanosheets prepared by a simple and scalable thermal exfoliation method. A wet chemistry approach was employed to produce heterojunctions for hydrogen gas evolution under solar light. The synergic effect achieved by combining both nanomaterials resulted in a H_2 production of 4593 μmol g^{-1} h^{-1} in correspondence of low loadings of $Cs_3Bi_2Br_9$ NCs in the composite. In conclusion, this work provides further evidence of lead-free MHPs as highly active materials for photocatalytic applications, with considerable potential in the clean energy research field.

 doi:10.20944/preprints202211.0524.v1

Table 1. HER values reported in the literature using lead-free perovskites/g-C3N4 composites.

Composite	HER/μmol g^{-1} h^{-1}	Experiment conditions	Ref
Bulk $Cs_3Bi_2Br_9$/bulk g-C_3N_4	1 050	1 $g_{catalyst}/L_{sol}$, 10 % *v/v* TEOA, 3 % *wt*. Pt, 500 W m^{-2}	[17]
Bulk PEA_2SnBr_4/bulk g-C_3N_4	1 600	1 $g_{catalyst}/L_{sol}$, 10 % *v/v* TEOA, 3 % *wt*. Pt, 500 W m^{-2}	[25]
Bulk $PhBz_2Ge_2Br_4$/bulk g-C_3N_4	1 200	1 $g_{catalyst}/L_{sol}$, 10 % *v/v* TEOA, 3 % *wt*. Pt, 500 W m^{-2}	[5]
Bulk $Cs_3Bi_2I_9$/bulk g-C_3N_4	920	1 $g_{catalyst}/L_{sol}$, 10 % MeOH, 1 % Pt, UV light irradiation at 355 nm.	[26]
Bulk $DMASnBr_3$/bulk g-C_3N_4	1 730	1 $g_{catalyst}/L_{sol}$, 10 % *v/v* TEOA, 3 % *wt*. Pt, 500 W m^{-2}	[27]
$Cs_3Bi_2Br_9$ NCs/g-C_3N_4 NSs	4 593	1 $g_{catalyst}/L_{sol}$, 10 % v/v TEOA, 3 % wt. Pt, 500 W m^{-2}	**This work**

Note: PEA, phenylethylammonium; PhBz, phenylbenzilammonium; DMA, dimethylammonium; NCs, nanocrystals; NSs, nanosheets; TEOA, triethanolamine; MeOH, Methanol.

Supplementary Materials: Figure S1: XRD pattern of the bulk g-C_3N_4 and the g-C_3N_4 nanosheets; **Figure S2:** SEM micrograph of the bulk g-C_3N_4; **Figure S3**: Absorbance spectra versus wavelength of the g-C_3N_4 NSs, the $Cs_3Bi_2Br_9$ NCs and the $Cs_3Bi_2Br_9$/g-C_3N_4 NSs composites produced at different percentages of perovskite loading (% *wt.*); **Figure S4:** BSE-HRSEM micrograph of the 0.44 % *wt.* $Cs_3Bi_2Br_9$ NCs/g-C_3N_4 NS.

Author Contributions: For research articles with several authors, a short paragraph specifying their individual contributions must be provided. The following statements should be used "Conceptual-ization, LM; methodology, MML.; formal analysis, MML, AS, AP, FP, FF, AL and LM; investigation, MML; writing—original draft preparation, MML and LM.; writing—review and editing, MML, AS, AP, FP, FF, AL and LM; supervision, LM; funding acquisition, LM. All authors have read and agreed to the published version of the manuscript."

Funding: The authors would like to thank to the CICOPS fellowship program of the University of Pavia for the scholarship provided to Maria Medina-Llamas. F.P and A.L. acknowledge Puglia regional council (Grant name: Perseo, CUP: H95F20000890003).

Data Availability Statement: "Not applicable".

Conflicts of Interest: The authors declare no conflict of interest."

References

1. Shi, M., et al., *Understanding the effect of crystalline structural transformation for lead-free inorganic halide perovskites.* Advanced Materials, 2020. **32**(31): p. 2002137.
2. Shyamal, S. and N. Pradhan, *Halide perovskite nanocrystal photocatalysts for CO2 reduction: successes and challenges.* The Journal of Physical Chemistry Letters, 2020. **11**(16): p. 6921-6934.
3. Medina-Llamas, M., et al., *Continuous Production of Metal Oxide Nanoparticles via Membrane Emulsification–Precipitation.* Industrial & Engineering Chemistry Research, 2020. **59**(19): p. 9085-9094.
4. Tasleem, S. and M. Tahir, *Current trends in strategies to improve photocatalytic performance of perovskites materials for solar to hydrogen production.* Renewable and Sustainable Energy Reviews, 2020. **132**: p. 110073.

5. Romani, L., et al., *Achieving Air/Water Stable and Photocatalytically Active Ge-Containing 2D Halide Perovskites by Organic Spacer Engineering*.
6. Wang, M., et al., *Remarkably enhanced hydrogen generation of organolead halide perovskites via piezocatalysis and photocatalysis.* Advanced Energy Materials, 2019. **9**(37): p. 1901801.
7. Carbon Nitride-Perovskite Composites: Evaluation and Optimization of Photocatalytic Hydrogen Evolution in Saccharides Aqueous Solution. A. Speltini, L. Romani, D. Dondi, L. Malavasi, A. Profumo. Catalysts 2020, 10, 1259; doi:10.3390/catal10111259.
8. Bresolin, B.-M., et al., *Pb-free Cs3Bi2I9 perovskite as a visible-light-active photocatalyst for organic pollutant degradation.* Nanomaterials, 2020. **10**(4): p. 763.
9. Akinbami, O., et al., *Lead-free Rudorffite-type Cs3Bi2Br9 nanoparticles for photocatalytic degradation of rhodamine B and methylene blue.* Journal of Photochemistry and Photobiology A: Chemistry, 2021. **419**: p. 113460.
10. Bhosale, S.S., et al., *Mechanism of photocatalytic CO2 reduction by bismuth-based perovskite nanocrystals at the gas–solid interface.* Journal of the American Chemical Society, 2019. **141**(51): p. 20434-20442.
11. Miodyńska, M., et al., *Lead-free bismuth-based perovskites coupled with g–C3N4: A machine learning based novel approach for visible light induced degradation of pollutants.* Applied Surface Science, 2022. **588**: p. 152921.
12. Song, K., et al., *Environmentally Stable Mesoporous g-C3N4 Modified Lead-Free Double Perovskite Cs2AgBiBr6 for Highly Efficient Photocatalytic Hydrogen Evolution.* Catalysis Letters, 2022: p. 1-10.
13. Lin, L., et al., *Tri-s-triazine-based crystalline graphitic carbon nitrides for highly efficient hydrogen evolution photocatalysis.* Acs Catalysis, 2016. **6**(6): p. 3921-3931.
14. Wu, C., et al., *Making g-C3N4 ultra-thin nanosheets active for photocatalytic overall water splitting.* Applied Catalysis B: Environmental, 2021. **282**: p. 119557.
15. Niu, P., et al., *Graphene-like carbon nitride nanosheets for improved photocatalytic activities.* Advanced Functional Materials, 2012. **22**(22): p. 4763-4770.
16. Miao, H., et al., *A novel strategy to prepare 2D g-C3N4 nanosheets and their photoelectrochemical properties.* Journal of Alloys and Compounds, 2017. **690**: p. 669-676.
17. Dong, X. and F. Cheng, *Recent development in exfoliated two-dimensional gC 3 N 4 nanosheets for photocatalytic applications.* Journal of Materials Chemistry A, 2015. **3**(47): p. 23642-23652.
18. A. Pisanu, A. Speltini, B. Vigani, F. Ferrari, M. Mannini, N. Calisi, B. Cortigiani, A. Caneschi, P. Quadrelli, A. Profumo, L. Malavasi, Enhanced hydrogen photogeneration by bulk g-C_3N_4 through a simple and efficient oxidation route. Dalton Trans. 2018, 47, 6772-6778.
19. Romani, L., et al., *Experimental Strategy and Mechanistic View to Boost the Photocatalytic Activity of Cs3Bi2Br9 Lead-Free Perovskite Derivative by g-C3N4 Composite Engineering.* Advanced Functional Materials, 2021. **31**(46): p. 2104428.
20. Veronese, A., et al., *Morphological and Optical Tuning of Lead-Free Cs2SnX6 (X= I, Br) Perovskite Nanocrystals by Ligand Engineering.* Frontiers in Electronics, 2021: p. 6.
21. fritsch-international. *Operating manual planetary micro mill pulverisette 7 classic line.* [cited 2022 30-March-2022]; https://www.fritsch-international.com/services/downloads-videos/?tx_downloads_pi1%5Bsubmitted%5D=true&tx_downloads_pi1%5Baction%5D=searchResult&cHash=29ce24277ee8306b540e801f76ad6016#downloadsearch].
22. Zhuang, S., et al., *Synthesis of nitrogen-doped graphene catalyst by high-energy wet ball milling for electrochemical systems.* International Journal of Energy Research, 2016. **40**(15): p. 2136-2149.
23. Protesescu, L., et al., *Low-cost synthesis of highly luminescent colloidal lead halide perovskite nanocrystals by wet ball milling.* ACS applied nano materials, 2018. **1**(3): p. 1300-1308.

 doi:10.20944/preprints202211.0524.v1

24. Luo, J., et al., *Efficient and stable emission of warm-white light from lead-free halide double perovskites.* Nature, 2018. **563**(7732): p. 541-545.
25. Guo, Z., et al., *Alignment of redox levels at semiconductor–water interfaces.* Chemistry of Materials, 2018. **30**(1): p. 94-111.
26. Ambrosio, F., G. Miceli, and A. Pasquarello, *Redox levels in aqueous solution: Effect of van der Waals interactions and hybrid functionals.* The Journal of Chemical Physics, 2015. **143**(24): p. 244508.
27. Romani, L., et al., *PEA 2 SnBr 4: a water-stable lead-free two-dimensional perovskite and demonstration of its use as a co-catalyst in hydrogen photogeneration and organic-dye degradation.* Journal of Materials Chemistry C, 2020. **8**(27): p. 9189-9194.
28. Bresolin, B.-M., et al., *Cs3Bi2I9/g-C3N4 as a new binary photocatalyst for efficient visible-light photocatalytic processes.* Separation and Purification Technology, 2020. **251**: p. 117320.
29. Romani, L., et al., *Water‐stable DMASnBr3 lead‐free perovskite for effective solar‐driven photocatalysis.* Angewandte Chemie, 2021. **133**(7): p. 3655-3662.